

Hydrocyclone-enhanced scalable photocatalytic hydrogen generation, from macroscale turbulence to nanoscale reaction dynamics

Received: 16 July 2025

Accepted: 20 January 2026

Published online: 29 January 2026

 Check for updates

Danhui Yang¹, Yizhou Yang¹, Fanghe Zhou¹, Zhuofan Deng¹, Chuanjie Cui², Jianping Li³✉, Pengbo Fu¹, Mingze Ma⁴, Wenjie Lv¹, Zhengdai Zhang¹, Xuejing Yang¹✉ & Hualin Wang¹✉

Photocatalytic hydrogen production faces barriers to industrialization, including inadequate light absorption and limited mass/momentum transfer at scale. Integrating external hydrocyclones into photoreactors is a promising solution, yet the multiscale complexity of hydrocyclone-driven hydrogen generation impedes mechanistic understanding and rational system design. Herein, we build a scalable hydrocyclone-based photoreactor that achieves 270 mL/h hydrogen yield and 5.26% solar-to-hydrogen efficiency under simulated sunlight, as 4.5 times higher than static conditions. We develop a hierarchical multiscale model combining computational fluid dynamics, solid mechanics and density functional theory, which connects macro-scale hydrocyclone flow strain to atomic-level photocatalytic processes. Here, we show that shear stress-induced nanoscale lattice restructuring of the catalyst modulates photoexcitation pathways, triggers a threshold-activated catalytic amplification effect, and identifies an optimal flow rate of 20–30 L/min. These findings reveal a multiscale force–chemical coupling mechanism linking reactor-scale hydrocyclone flow fields to lattice-scale strain-driven catalytic enhancement, guiding large-scale photocatalytic hydrogen production.

In the pursuit of renewable energy utilization and carbon neutrality, photocatalytic hydrogen production has emerged as a promising approach for generating green hydrogen through sustainable processes^{1–3}. While significant progress has been made in laboratory settings,⁴ industrial deployment remains the crucial next step toward achieving global decarbonization goals.^{5,6} This transition requires efficient, large-scale reactor systems, leading to the development of various reactor configurations, including slurry,⁷ tubular,⁸ fluidized bed,⁹ and panel¹⁰ designs. Among these configurations, panel systems

have achieved notable success with 100 m² demonstration facilities, marking an important advancement from laboratory research toward practical applications.¹¹ Despite such promising progress, photocatalytic hydrogen technologies universally face scalability challenges at larger scales: mass transfer inefficiencies,¹² suboptimal light utilization,¹³ and catalyst deactivation during extended operation.¹⁴ These limitations arise primarily from the traditional geometric similarity scale-up paradigm,^{15,16} This approach requires maintaining geometric similarity while enlarging reactor dimensions, but fails to

¹National Engineering Research Center of Industrial Wastewater Detoxication and Resource Recovery, East China University of Science and Technology, Shanghai, China. ²Department of Engineering Science, University of Oxford, Oxford, UK. ³College of Carbon Neutrality Future Technology, Sichuan University, Chengdu, PR China. ⁴College of General Aviation and Flight, Nanjing University of Aeronautics and Astronautics, Liyang, China.

✉ e-mail: lijianping1016@scu.edu.cn; xj.yang@ecust.edu.cn; wanghl@ecust.edu.cn

account for the non-linear scaling behavior of heat and mass transfer phenomena, resulting in deteriorated performance as reactor size increases.¹⁷ Therefore, developing large-scale reaction systems based on alternative scale-up strategies has become essential for overcoming these inherent scaling limitations, unlocking the industrial potential of photocatalytic hydrogen production, and ultimately enabling the commercial deployment of artificial photosynthesis technologies for sustainable energy applications.¹⁸

Hydrocyclone technology offers a promising alternative scale-up approach,¹⁹ employing a fundamentally different numbering-up strategy.²⁰ Unlike conventional reactors that rely on geometric enlargement, hydrocyclones achieve large-scale processing capacity through parallel arrangement of multiple units, allowing for linear superposition of individual unit performance while maintaining operational efficiency.²¹ This approach offers significant potential for minimizing scale-up effects in large-scale photocatalytic hydrogen production applications. Originally developed for particle classification and separation,²² hydrocyclones have evolved into powerful process intensification devices for enhancing reaction and mass transfer processes, with applications extending to absorption,²³ sludge activation,²⁴ heat exchange,²⁵ synthesis,^{26,27} and catalysis.^{28,29} However, despite broad adoption as separation units, hydrocyclones are seldom treated as active reactors: systematic exploitation of their high-shear and negative-pressure core to drive hydrodynamic-chemical (force-chemical) coupling for catalytic enhancement remains scarcely addressed. Against this backdrop, the intense swirling flow and high shear forces within hydrocyclones provide an ideal platform for implementing strain engineering strategies at the catalyst level.³⁰ These mechanical forces cause lattice distortions, which alter the electronic structure,³¹ enhance surface active site reactivity, and modify charge-transfer properties in catalytic material,³² thereby improving overall catalytic performance. Despite this potential, realizing the full benefits of this strain-enhanced approach faces a significant theoretical bottleneck: the absence of a comprehensive multiscale modeling framework capable of bridging macroscale fluid dynamics ($>10^{-1}$ m) with nanoscale electronic phenomena ($<10^{-8}$ m). This gap persists because current strain engineering focuses narrowly on material-scale modifications, such as introducing defects to manipulate microscopic stress.³³ Such single-scale approaches overlook the essential hierarchical coupling from reactor-scale hydrodynamics to molecular-level electronic structure, creating a major barrier to the rational design and scale-up of hydrocyclone-based photocatalytic systems.

Here, we present a scalable hydrocyclone-based photoreactor for photocatalytic hydrogen production and establish the corresponding multiscale modeling framework. Using pre-synthesized spherical TpPa-COF supported Pt NPs (Pt-COF) photocatalysts, our hydrocyclone flow field implementation achieves a 4.5-fold enhancement in hydrogen production efficiency compared to static systems, with stable solar-to-hydrogen energy conversion over 42 h of continuous operation. In this work, we develop a comprehensive hierarchical multiscale modeling framework for hydrocyclone reactors using a force-chemical multiphysics approach that systematically integrates experimental observations with theoretical modeling. This framework bridges the scale gap from macroscopic fluid dynamics to nanoscale electronic phenomena, revealing the key cross-scale mechanisms in hydrocyclone-flow photoreactors and elucidating the intricate interplay between macroscale fluid-induced forces and nanoscale catalyst electronic structure. By systematically linking computational fluid dynamics at the macroscale, continuum mechanics at the mesoscale, and quantum mechanical analysis at the nanoscale, where each scale provides boundary conditions for the subsequent level, we uncover the mechanism by which mechanical forces enhance catalytic performance through lattice distortions and improved charge separation (Fig. S1). These mechanistic insights provide guidance for scaling hydrocyclone reactors and a versatile framework for designing other

large-scale photocatalytic systems. Our work enriches the concept of strain engineering, shifting from traditional, single-scale material modifications to integrated control of multiscale phenomena. We demonstrate that macroscopic force fields can be systematically engineered to boost catalytic performance, supporting the development of scalable hydrogen production.

Results

Reaction performance of hydrocyclone-based photocatalytic hydrogen production reactor

The three-dimensional layout of the hydrocyclone-based photocatalytic hydrogen production system is shown in Fig. 1a, along with a sectional view of the internal structure of the reaction chamber (more details about the reactor can be found in Fig. S2 and S3). The hydrocyclone photocatalytic reactor operating continuously at a flow rate of 40 L/min is shown in Fig. 1b, while the hydrogen collecting process using an airtight syringe at intervals of 30 minutes can be viewed through Supplementary Movie 1. The apparatus contains two primary circulation loops: a cooling water loop and a photocatalytic fluid loop. In this system, the cooling water loop, maintained constantly at 4 °C by the cooling water circulator, ensures stable temperature control for the reactor. The reaction solution was able to maintain a stable temperature of 30 ± 1 °C with the help of a cooling system to exclude local thermal effects (Fig. S4). The photocatalytic fluid loop includes the hydrocyclone reaction chamber and associated circulation piping, which together contain a total of 18 L catalyst-containing liquid. The hydrocyclone reaction chamber is fabricated from 316 stainless steel and consists of a 200 mm cylindrical section (height=200 mm) transitioning into a conical section with a 30° apex angle, terminating in a 25 mm underflow orifice. Two tangential feed inlets are positioned along the chamber wall to induce a high-intensity hydrocyclone flow, while a dedicated outlet at the top of the chamber facilitates hydrogen collection. A 500 W long-arc Xenon lamp is centrally mounted within the reactor and is housed within an AML5G-filtered glass enclosure to simulate solar irradiation. During operation, the fluid pump provides the driving force for hydrocyclone flow generation, ensuring vigorous mixing and enhanced momentum and mass transfer. Compared to typical laboratory-scale hydrocyclone reactors (typically 10–50 mm diameter, 0.1–2 L volume),³⁴ our 200 mm diameter system with 18 L processing volume represents a significant scale-up achievement. Furthermore, the modular design enables further scaling through parallel arrays or proportional enlargement, providing clear pathways for industrial deployment.

Using a hydrocyclone-based photocatalytic reactor, we conducted the systematic study on the relationship between fluid flow rate and hydrogen evolution performance under a fixed catalyst loading concentration of 30 mg/L (Fig. 1c). As the flow rate increased from 0 to 40 L/min, the hydrogen yield rose steadily from 2.71 ± 0.18 mmol/h at 0 L/min to 12.03 ± 0.27 mmol/h at 40 L/min, corresponding to 4.5 times the initial yield. Based on hydrogen production data at 40 L/min, the apparent quantum yield (AQY) at 420 nm was calculated to be 12.7%. We also performed measurements and evaluated hydrogen production at a fixed flow rate of 40 L/min across various catalyst concentrations, through the hydrocyclone-based photocatalytic reactor (Fig. S5). As the catalyst concentration increased, the overall hydrogen evolution rate rose but ultimately plateaued at higher loadings. Meanwhile, the catalyst utilization efficiency, improved initially and reached a peak of $22.35 \text{ mmol} \cdot \text{h}^{-1} \cdot \text{g}^{-1}$ with the catalyst loading of 30 mg/L, followed by a decline at higher concentrations. From a practical perspective, excessive catalyst loading not only raises operational costs but also poses a risk of clogging the circulation system.³⁵ Consequently, 30 mg/L was selected as the optimal catalyst concentration for further experiments.

We conducted on-off cycling experiments of the hydrocyclone at various flow rates to verify the impact of the hydrocyclone flow field on

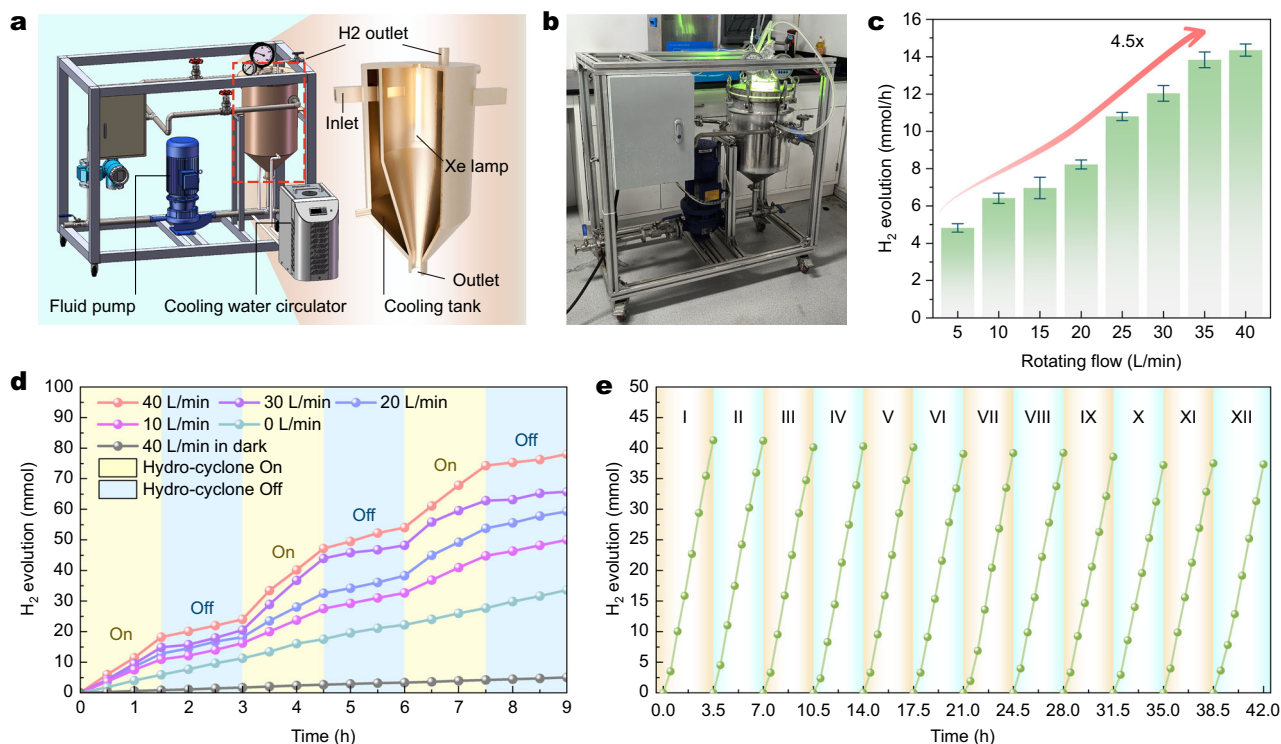


Fig. 1 | Hydrocyclone-enhanced photocatalytic hydrogen evolution. **a** Device layout of hydrocyclone-based photocatalytic hydrogen production reactor. **b** Hydrocyclone-based photocatalytic reactor in operation. **c** Hydrogen production comparison at a fixed catalyst concentration of 30 mg/L under different flow rates. The red arrow indicates an overall 4.5-fold increase in hydrogen evolution as the

rotating flow rate increases. The error bars in the figure were calculated using data from three parallel experiments. **d** Hydrocyclone on-off cycling experiment at a catalyst concentration of 30 mg/L under varying flow rates, with each cycle running for 1.5 h on and 1.5 h off, repeated three times. **e** Long-term operation test of the hydrogen production device, continuously running for 42 h.

hydrogen production (Fig. 1d). The pale yellow and pale blue regions each represents one full on-off 3 h cycle of the hydrocyclone, during which hydrogen production was recorded every 30 min. The cyan-colored curve denotes the baseline, where the hydrocyclone remained off throughout the entire experiment. The hydrogen production recorded under hydrocyclone on-off cycles at flow rates of 10, 20, 30, and 40 L/min are shown as the four additional curves above the base line. Notably, the hydrogen production rate exhibited a marked response to the hydrocyclone: its presence significantly enhanced hydrogen evolution, whereas its absence rapidly restored the system to baseline levels. Furthermore, we performed a control experiment at 40 L/min with the hydrocyclone but without illumination. Under these dark conditions, the hydrogen yield was negligible, demonstrating that the energy input is originated from light rather than mechanical pumping. At a flow rate of 40 L/min, the long-term stability of the photocatalytic system was verified through a 42 h (12-cycle) test, with each cycle lasting 3.5 h (Fig. 1e). The hydrogen yield remained highly stable, exhibiting only about a 9.5% decline from the 1st to the 12th cycle. When compared with recent state-of-the-art systems (Fig. S29 and Table S3)^(11,36–45), our design overcomes the common trade-off between hydrogen production rate and photocatalytic efficiency. According to the IEA and U.S. DOE, a minimum of 5% STH is required for solar H₂ to compete economically with conventional energy technologies—an objective that planar-reactor configurations have yet to meet.⁴⁶ In contrast, the hydrocyclone flow regime presented here delivers markedly enhanced photon utilization and clearly demonstrates strong potential for commercial deployment.

Characterization of Pt-loaded COF catalysts

We selected Pt-loaded TpPa-COF particles due to their exceptional suitability for photocatalytic applications. TpPa-COF is characterized by its high porosity, tunable bandgaps, periodic organic frameworks,

and broad visible-light absorption, which collectively contribute to its outstanding performance. Previous researches have demonstrated a scalable and economically-viable emulsion polymerization method for fabricating spherical TpPa-COF particles with tunable morphological characteristics.⁴⁷ This optimized protocol achieves single-batch yields at the gram scale while preserving stringent control over particle architecture, thereby addressing the critical catalyst supply chain requirements for sustained pilot-scale experimental operations. Pt-COF particles were prepared through the Schiff base reactions of 1,3,5-triformylphloroglucinol (Tp) with p-phenylenediamine (Pa) and subsequent photodeposition of Pt nanoparticles (NPs) onto the COF framework (Fig. 2a and Fig. 2b). To further elucidate the chemical nature of the Pt NPs deposited on the COF surface, we conducted a series of structural and spectroscopic characterizations. As shown in Fig. 3c, TEM images reveal well-dispersed Pt NPs on the COF substrate. By controlling the light-deposition reaction time, both the sizes and densities of the Pt NPs can be effectively tuned. EDS mapping (Fig. S6) shows a uniform distribution of Pt, and the representative catalyst contains ~1 wt% Pt. This loading is consistent with AC HAADF-STEM images (Fig. 2d), which reveal 10–20 nm Pt domains dispersed on the COF surface. High-resolution TEM (HRTEM) measurements (Fig. 2e) show a lattice spacing of 0.23 nm, matching the (111) crystallographic plane of metallic Pt.

The comparison between powder X-ray diffraction (XRD) patterns of pristine COF and Pt-loaded COF (Fig. 2f) confirm that the minor Pt loading does not alter the primary crystalline phase of the COF. Meanwhile, the high-resolution X-ray photoelectron spectroscopy (XPS) spectra of N 1s and Pt 4f (Fig. S7) provide further evidence for the existence of metallic Pt in the sample. The N 1s spectrum displays a strong peak at 399.4 eV and a weaker one at 402.8 eV, corresponding to C-NH_x groups and π-excitations, respectively.⁴⁸ In the Pt 4f region, peaks at 71.6 eV and 74.9 eV are attributed to Pt-Pt bonds in metallic

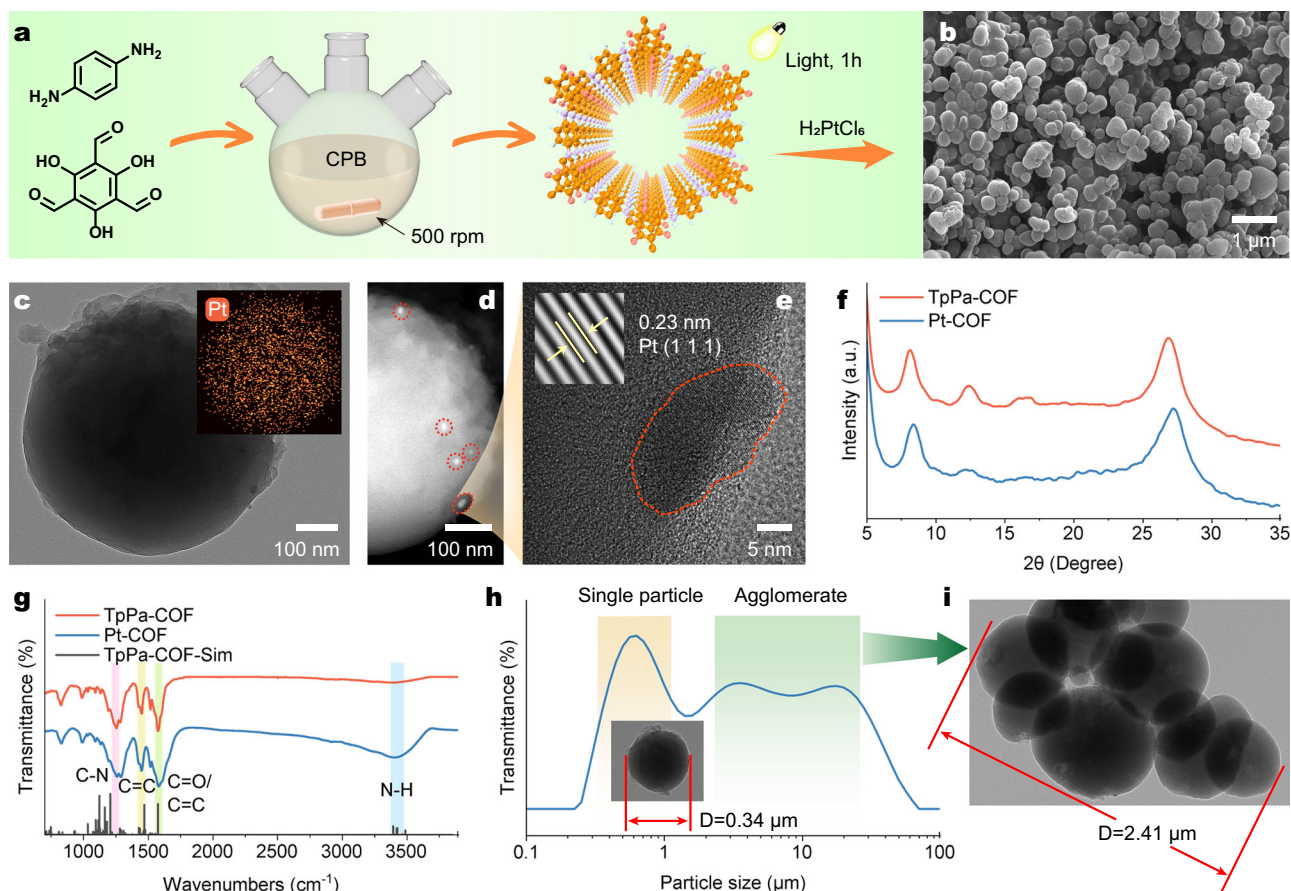


Fig. 2 | Structure of Pt-COF. **a** Schematic illustration of the preparation of spherical TpPa-COF via emulsion polymerization and the subsequent photodeposition of Pt NPs. **b** SEM image of the synthesized Pt-COF. **c** TEM image of a single Pt-COF sphere and the EDS elemental mapping (the insert image) of Pt. **d** STEM dark-field image of Pt-COF. **e** HRTEM image showing Pt NPs distributed on the COF surface.

f XRD patterns of Pt-COF and TpPa-COF. **g** FTIR spectra of Pt-COF and TpPa-COF along with simulated IR absorption peaks of TpPa-COF. **h** Malvern laser particle size analysis showing the particle dispersion in the actual reaction solution. The yellow and green shaded regions indicate the single-particle and agglomerate ranges, respectively. **i** TEM image of catalyst particle aggregation.

Pt⁰. Complementarily, FTIR spectra of Pt-loaded and pristine COFs (Fig. 2g) confirm the key framework functional groups, and in parallel solid-state ¹³C NMR verifies successful COF formation with characteristic β-ketoenamine linkages (Fig. S8). Finally, N₂ sorption/BET analysis (Fig. S9) reveals a surface-area decrease upon Pt loading (from 964.0 to 475.9 m²/g), consistent with partial micropore blocking by deposited Pt NPs.

To further elucidate the behavior of catalyst microparticles in fluid and to reveal the meso- and micro-scale evidence underpinning our theoretical framework, we collected random liquid samples from the reactor after 24 h of continuous operation. As shown in Fig. 2h, the primary peak is centered at ~0.6 μm (highlighted in yellow), corresponding to individual catalyst particles freely dispersed in the liquid. Meanwhile, the secondary peaks spanning 2 μm–30 μm (highlighted in green) signify larger agglomerates. Volume-weighted PSDs of the reaction slurry at 8, 16, and 24 h (Fig. S10) show a time-dependent increase in single/small-agglomerate fractions and a decrease in large agglomerates, indicating that the hydrocyclone's high-shear, rapid recirculation suppresses agglomeration. This suppression is consistent with the sustained performance observed over extended operation. TEM images (Fig. 2i) directly capture these aggregates in the liquid phase, illustrating that several to dozens of spherical particles can stack together—under the influence of fluid flow—into larger agglomerates. Concurrently, XRD (Fig. S11) and XPS analyses (Fig. S7) conducted prior to and following extended hydrocyclone operation revealed no occurrence of new phases or discernible binding energy

shifts, thereby substantiating the structural and chemical stability of the Pt-COF. The above observation results reveal the macroscopic movement of the particles driven by external fluids and the microscopic characteristics of TpPa-COF catalysts. However, it remains essential to perform further analysis based on multi-scale theoretical model to construct the connection between the two across scales.

Multiscale modeling: from reactor flows to lattice distortion

To elucidate the multiscale force-chemical interactions bridging the macroscopic reactor flow dynamics with the nanoscale electron-hole separation phenomena, a comprehensive investigation of particle motion and deformation patterns within the hydrocyclonic field is imperative. However, given the inherent challenges in direct tracking of micrometer-scale catalyst dynamics, hydrogel spheres were employed as tracer particles to enable qualitative assessment of fluid shear-induced deformations under hydrocyclonic conditions. The sodium-alginate polymer tracers were density-matched to the catalyst particles. Because their elastic modulus is lower than that of the COF particles, they permit qualitative evaluation of shear-induced deformation in the hydrocyclone while maintaining catalyst-like flow behavior.⁴⁹ These tracer particles were strategically introduced into a transparent scale-matched hydrocyclone (structurally identical to the operational system) operated at 40 L/min, enabling direct visual tracking of their translational-rotational kinematics and morphological evolution via high-speed photogrammetry (Fig. 3a; and Supplementary Movie 2).

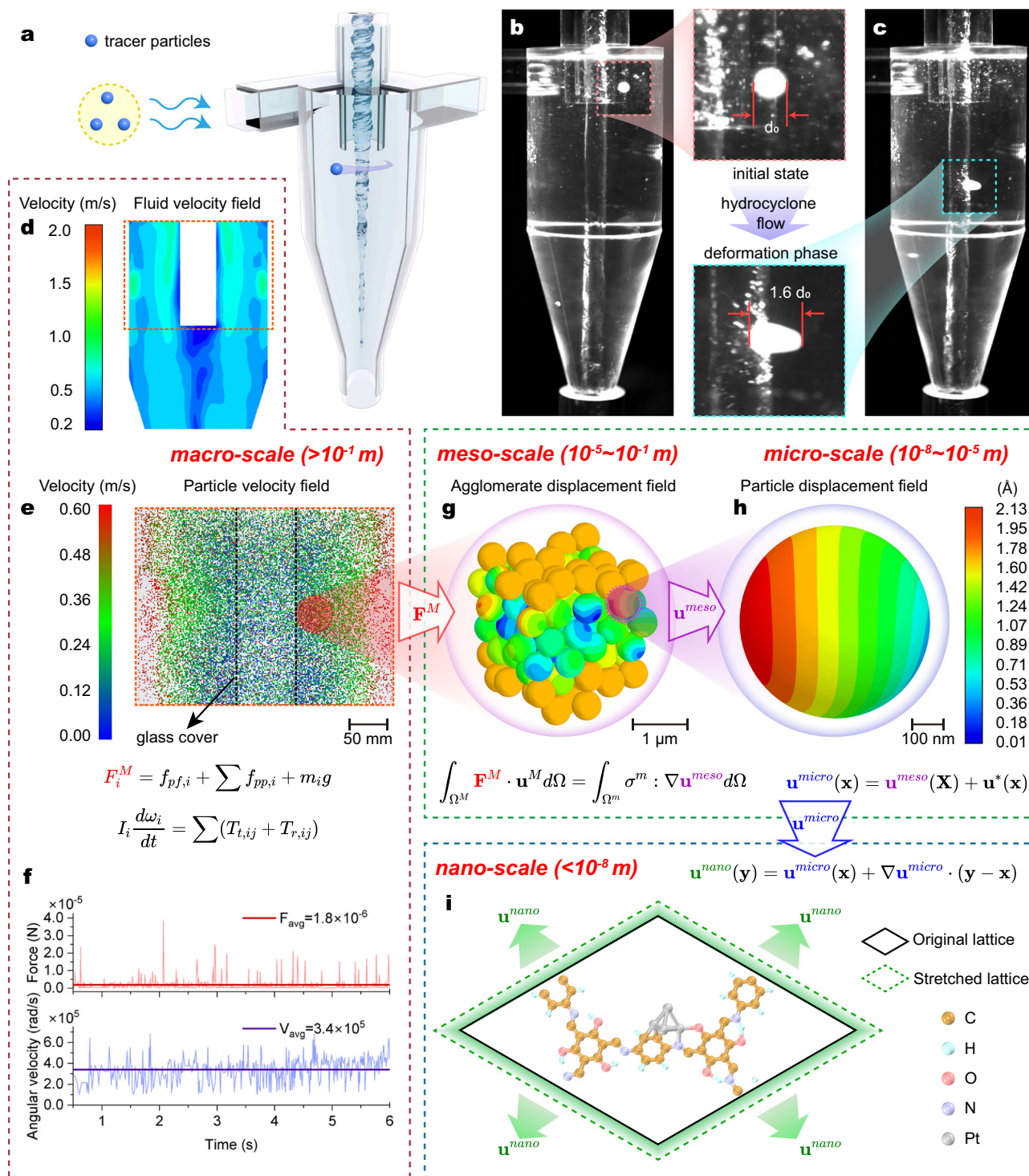


Fig. 3 | Hierarchical multiscale modeling from macro- to nano-scale.

a Schematic illustration of tracer particle motion in the hydrocyclone. **b** High-speed image of the tracer particle at the hydrocyclone column section without significant deformation. **c** High-speed image showing the stretching deformation of the tracer particle after being captured by the central negative pressure zone. **d** CFD simulation of the cross-sectional view of the fluid velocity distribution in the reactor.

e CFD-DEM simulation of the velocity field of agglomerated particles in the main light absorption region. **f** Variation of average force and rotational speed over time. **g** Meso-scale displacement field of agglomerates. **h** Micro-scale displacement field of sub-particles. **i** Lattice distortion at the nano-scale induced by micro-scale displacement.

Figures 3b, c present high-speed camera snapshots of the tracer particles as they enter the cylindrical section and subsequently the conical section of the hydrocyclone, where they are entrained by the central low-pressure zone. In the cylindrical section, the particles remain near the hydrocyclone wall, experiencing minimal fluid shear

forces; hence, the particle retains a nearly spherical shape with negligible deformation. Under the influence of gravity along the vertical axis, their overall motion follows a helical downward path. Upon transitioning into the conical section and being captured by the central low-pressure zone, the particles begin to ascend. At this point, their

tangential velocity increases sharply, exposing them to intensified shear forces and centrifugal effects. Consequently, the particles undergo pronounced elongation, transforming into an ellipsoidal shape of which the major-axis diameter is 1.6 times that observed in the cylindrical section. These high-speed imaging results offer direct qualitative evidence of the tensile deformation experienced by particles within the flow field.

Building on the high-speed imaging experiments with tracer spheres, we next establish how forces transfer from the macro-scale flow field to the meso-/micro-/nano-scale lattice of the catalyst. To capture this force-transmission pathway, we adopt a hierarchical multiscale modeling framework, wherein the hydrocyclone flow field is analyzed in four scales: (i) macro-scale ($>10^{-1}$ m), representing the overall dimensions of the hydrocyclone; (ii) meso-scale (10^{-5} – 10^{-1} m), encompassing aggregated particle clusters; (iii) micro-scale (10^{-8} – 10^{-5} m), focusing on individual particles; and (iv) nano-scale ($<10^{-8}$ m), probing lattice-level phenomena. The hierarchical multiscale method, frequently employed in mechanics, partitions a structure into distinct scales so that simulation outcomes at one scale can serve as boundary conditions or material parameters for the next.⁵⁰ A multiscale approach becomes essential when micro- or nano-scale properties significantly influence macro-scale performance, and when physical processes across different scales strongly interact or couple.⁵¹ Here, we extend this methodology to a force-chemical coupling system, wherein the microstructural features of the catalyst markedly affect the macro-scale hydrogen production rate. Consequently, the hierarchical model provides a coherent framework to bridge observations from the hydrocyclone flow field at the reactor level down to the catalyst lattice interactions at the nano-scale level.

At the macro-scale level (Figs. 3d, e), the coupled computational fluid dynamics-discrete element method (CFD-DEM) approach is employed to simulate the motion and forces acting on catalyst agglomerates in a two-phase flow system consisting of a macroscopic fluid field and aggregated particle clusters. Using this integrated CFD-DEM framework, we constructed a hydrocyclone model mirroring the actual reactor geometry at an inlet flow rate of 40 L/min. Figure 3d depicts the cross-sectional view of the fluid velocity distribution in the reactor. The area outlined by the orange dashed box represents the primary reaction zone of the photocatalytic process. The central white rectangle denotes the optical filter cover, which serves to protect the light source and simulate the solar spectrum. Based on flow field data and particle size distribution analysis, an aggregate model was established and coupled with the flow field model to simulate the dynamic behavior of aggregated particle clusters within the hydrocyclone. This approach enables the visualization of particle velocities within the primary light absorption region. Evidently, particles adjacent to the reactor wall demonstrate significantly higher tangential velocities, reaching up to 0.60 m/s, while those near the lamp cover exhibit substantially reduced mobility. A pronounced particle accumulation is observed surrounding the lamp cover, attributed to the trapping mechanism of the central low-pressure vortex. Figure 3f quantitatively illustrates the temporal evolution of both the average rotational velocity (V_{avg}) and the average force (F_{avg}) acting on particles within this domain. Under simulated conditions at 40 L/min, the combined effects of swirling flow shear forces yield an average particle spin rate of 3.4×10^5 rad/s with a concurrent hydrodynamic force of 1.8×10^{-6} N. These derived F_{avg} values are subsequently implemented in our hierarchical multiscale framework, informing the subsequent mesoscale particle agglomeration model.

At the meso-scale level (Fig. 3g), the force $F^M = F_{avg}$ is applied as a boundary condition on the particle agglomeration. A representative region with 119 sub-particles was selected as a Representative Volume Element (RVE) for the meso-scale finite element modeling (FEM).⁵² According to the principle of work balance between the macro-scale

and meso-scale, we have:

$$\int_{\Omega^M} F^M \cdot u^M d\Omega = \int_{\Omega^m} \sigma^m : \nabla u^{meso} d\Omega \quad (1)$$

where Ω^M is the macro-scale domain, F^M is the macro-scale force vector, u^M is the macro-scale displacement field, Ω^m is the meso-scale domain, σ^m is the meso-scale stress tensor, u^{meso} is the meso-scale displacement field, ∇u^{meso} is the displacement gradient tensor at the meso-scale, and “:” denotes the double-dot product (tensor contraction) between two second-order tensors.

At the micro-scale level (Fig. 3h), we employed micromechanics theory to calculate the displacement field $u^{micro}(x)$ of one single catalyst particle. The meso-scale displacement $u^{meso}(X)$ computed at the upper scale is taken as the average boundary condition for the micro-scale model. The total micro-scale displacement field, u^{micro} , is thus composed of the large-scale mean displacement plus a small-scale perturbation:

$$u^{micro}(x) = u^{meso}(X) + \hat{u}^*(x) \quad (2)$$

where $\hat{u}^*(x)$ is the small-scale displacement perturbation that captures local microstructural deformation.

Finally, at the nano-scale level (Fig. 3i), an ab initio molecular dynamics (AIMD) model was constructed. The lattice expansion displacement, u^{nano} , can be derived from the micro-scale displacement by:

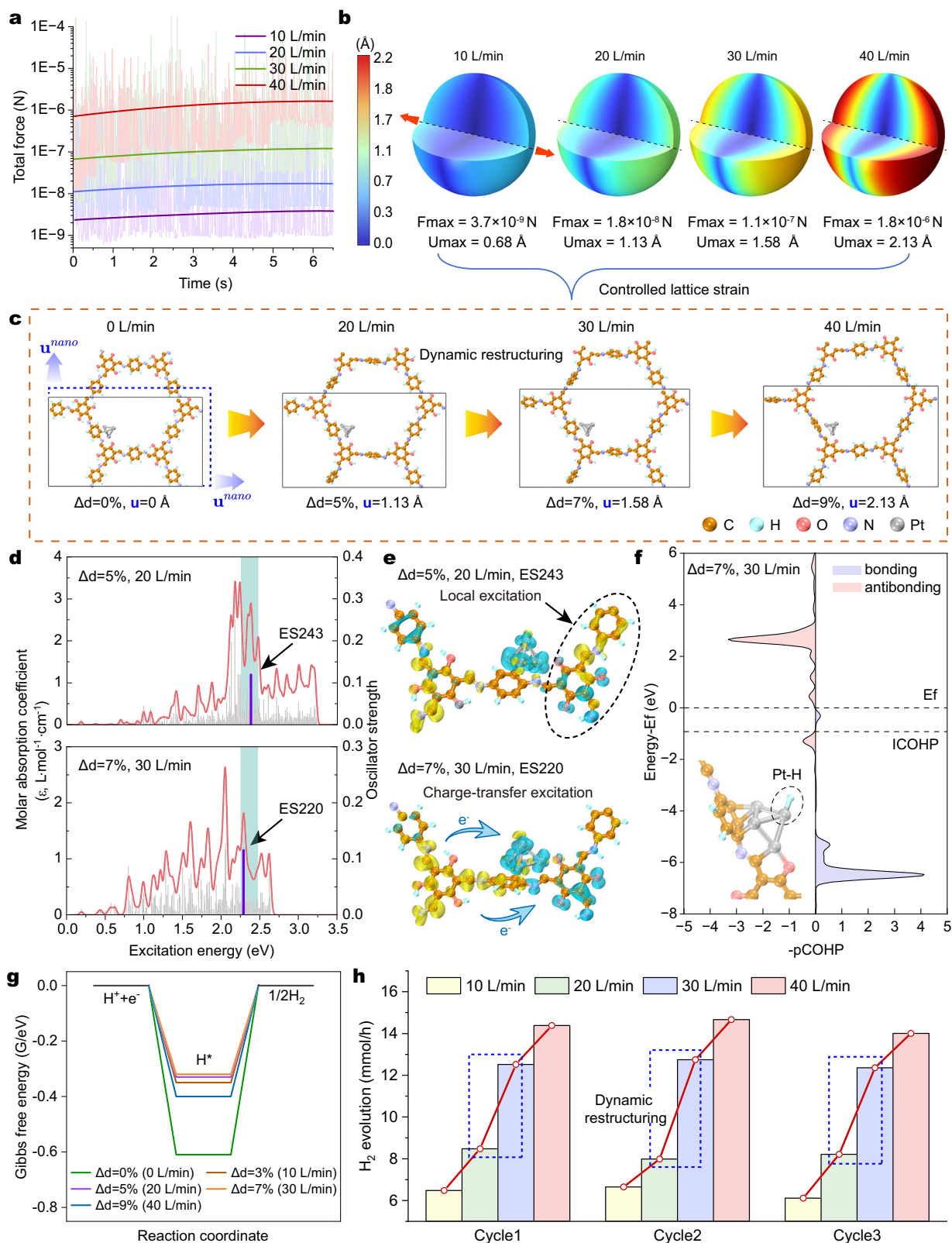
$$u^{nano}(y) = u^{micro}(x) + \nabla u^{micro} \cdot (y - x) \quad (3)$$

where $u^{nano}(y)$ is the nano-scale displacement field, ∇u^{micro} is the displacement gradient at the micro-scale, and $(y - x)$ denotes the relative position vector from x to y .

This multiscale formulation effectively quantifies lattice distortion through Newtonian potential field simulations, yielding u^{nano} of 2.13 Å under hydrodynamic flow conditions at 40 L/min. By employing this hierarchical and multiscale scheme, the macro- and meso-scales are connected through the flow field, the meso- and micro-scales via strain transfer, and the micro- and nano-scales through displacement. Crucially, the formulation establishes an explicit load-transfer pathway from reactor-scale hydrodynamics (CFD-DEM) to nanoscale lattice states (density functional theory, DFT): hydrodynamic velocity/pressure fields define mesoscopic stress boundary conditions (FEM), which are propagated as resolved strain/displacement fields to the atomistic model. As a result, the method specifies the strain conditions imposed on the AIMD lattice model, enabling a detailed exploration of how lattice deformation influences photocatalytic hydrogen evolution.

Lattice restructuring under strain and photocatalysis enhancement

To help better understanding the atomic-scale origin of strain-induced photocatalytic enhancement, we use density functional theory calculations, which are interpreted to provide qualitative trends rather than quantitative predictions under catalytic operating conditions. Conventional ground-state DFT band structures (Fig. S13) and densities of states (Fig. S14) show that Pt NPs loading introduces abundant hybrid states near the Fermi level (close to the valence-band maximum) as well as isolated in-gap levels, these states initiate HER by providing electron-accepting sinks at the COF-Pt junction. To further rationalize the experimentally observed strain-enhanced activity, we performed hierarchical multiscale modeling to quantify the strain-transmission pathway from the macroscale to the nanoscale. Figure 4a quantifies the peak hydrodynamic shear forces acting on catalyst particles in the hydrocyclone, revealing a two-order-of-magnitude increase from 3.7×10^{-9} N at 10 L/min to 1.8×10^{-6} N at 40 L/min, accompanied by a concomitant rise in particle strain. Crucially, Fig. 4b bridges multiscale



lattice distortion mechanisms by mapping flow-induced particle displacement fields. At flow rates spanning 10–40 L/min, the maximum single-particle displacement increases from 0.68 Å to 2.13 Å, directly quantifying hydrocyclone-induced tensile strain accumulation. The pronounced flow-rate dependency of the strain confirms localized stress concentration at catalyst edges, which is a critical prerequisite for the tensile lattice distortions observed in AIMD simulations.

To elucidate the influence of strain on the molecular structure of the COF, we investigated the crystal stability and the chemical environment changes of catalytic sites under the strain. Informed by prior work on few-atom Pt ensembles in photocatalysis, we model the COF–Pt junction using a Pt_4 interfacial surrogate to resolve site-specific, strain-sensitive electronic responses at under-coordinated motifs, rather than reproducing the global morphology of >10 nm Pt (1 1 1)

Fig. 4 | Hierarchical multiscale mechanism of lattice restructuring and HER enhancement. **a** Variations in the maximum hydrodynamic forces exerted on catalyst particles within the hydrocyclone under different flow rates. **b** Simulated displacement fields for a single catalyst particle under flow-induced shear forces. **c** AIMD simulated structural reshaping of the COF support under incremental tensile strain, while brown, cyan, red, purple, and silver spheres represent C, H, O, N, and Pt atoms respectively. **d** Calculated molar absorption spectra. The cyan band indicates the experimentally strongest absorption window, and the purple bar

highlights the excitation state with the highest oscillator strength within this band. **e** TDDFT-calculated electron-hole redistribution upon lattice distortion, where areas in cyan represent electron density increase and yellow represent holes. The blue arrow indicates the direction of electron migration. **f** COHP analysis of Pt–H bonding in the 7% lattice-distorted configuration. **g** Reaction free energies for H adsorption at the top site of the Pt NPs under different lattice strains. **h** Reproducible hydrogen production rate enhancement (20 → 30 L/min) across three operational cycles.

particles This surrogate is chemically relevant and computationally tractable, and it preserves the polarization physics central to our photoinduced mechanism.⁵³ Specifically, we constructed a theoretical model of a TpPa-COF loaded with a Pt₄ NPs and performed AIMD simulations (Supplementary Movie 3) for biaxial lattice strain ratios varying from 0% up to 11%, which corresponds to a maximum lattice elongation of ~2.6 Å. Key strain points during the AIMD simulation (Fig. 4c) reveals how COF structure changes during the lattice strain Δd increasing from 5% (1.13 Å) to 9% (2.13 Å). It has been demonstrated that by tracking the evolution of Pt's positional coordination, it is possible to ascertain that initially, Pt atoms predominantly adopt a Pt–N coordination configuration (with an average Pt–N bond length of ~2.1 Å), consistent with κ^2 - (N, O) binding of the COF linker. Under 5% in-plane strain, the Pt₄ NPs undergoes a gradual ligand rearrangement toward Pt–C coordination (average Pt–C bond length \approx 2.0 Å), consistent with the evolving interfacial environment (Fig. S15). When $\Delta d = 11\%$, the COF aromatic ring network fractures (Fig. S16). The potential energy (Fig. S17) and conserved quantity traces (Fig. S18), together with the time-resolved Pt–N/Pt–C bond-length fluctuations (Fig. S19), quantify these strain-dependent transitions. This alteration in coordination field can significantly impact the photocatalytic hydrogen production. Fig. S20 reveals that, at the ground state, the differential charge density shows a net electron transfer from the Pt₄ NPs to the COF, corresponding to a built-in electric field, which then can be beneficial for subsequent electron transfers from COF to Pt upon the photophysical processes.⁵³

Based on the configuration obtained by the AIMD simulation, we performed time-dependent DFT (TD-DFT) calculations under the Tamm-Dancoff approximation (TDA) to probe strain-dependent photoexcitation dynamics by comparing two meta-stable configurations at 5% strain and 7% strain (Fig. 4d),^{54,55} Targeting the experimentally identified UV-vis absorption (500–550 nm, 2.25–2.48 eV; Fig. S21) governing photocatalytic efficiency, we analyzed the highest oscillator strength states: ES243 at 5% strain (2.38 eV) and ES220 at 7% strain (2.29 eV), which dominated the light absorption within each spectral section. Electron-hole pair analysis (Fig. 4e) revealed a critical transition in excitation mechanisms between these states. For the 5%-strained configuration (ES243) with intact Pt–N coordination, the system exhibited a hybrid charge-transfer/local excitation (CT/LE) character, where partial electron transfer occurred from COF phenyl rings to Pt NPs alongside residual LE in the COF framework. Under 7% tensile strain, the Pt coordination environment shifts from initial Pt–N σ -bonds to strain-stabilized Pt–C coordination accompanied by interfacial π^* orbital hybridization between Pt NPs and the COF scaffold. The strained state (ES220) displayed complete ligand-to-metal charge-transfer (LMCT) behavior with full spatial charge separation: holes localized on COF ligands and electrons concentrated at Pt sites. Additionally, we analyzed pristine TpPa-COF and a low-strain Pt-COF (3%) reference and found predominantly local excitations in both cases (Fig. S22). Thus, Pt loading is necessary to provide electron-acceptor states, whereas tensile strain amplifies the separation; together they couple to enable efficient electron-hole splitting. Subsequently, the d - π hybridization between Pt and COF stabilizes this carrier separation lifetime, thereby greatly enhancing the photocatalytic performance. Moreover, reconstruction for the coordination of Pt under the strain

remarkably minimizes the exciton recombination losses, resulting in the enhanced photon utilization.

To connect the excited-state picture with steady-state reactivity, we first examined the ε_d descriptors under strain (Fig. S23). As shown in Fig. S24(a), ε_d increases approximately linearly with strain up to ~7%, but turns over at 9%. In the same strain range, ΔG_H co-varies with ε_d broadly consistent with the classic d -band picture. Notably, the ~7% case deviates from the linear trend: although ε_d is upshifted, ΔG_H becomes larger (Fig. S24b). These results indicate that, while the d -band descriptor tracks the activity trend at modest strain, it becomes insufficient at larger strain. Therefore, it is necessary to provide more direct evidence via thermodynamic H-adsorption calculations on Pt sites. Further theoretical studies reveal that, the enhancement of the photocatalytic performance is attributed to the hydrogen adsorption-desorption behavior changes by the strains. First, ESP calculations (Fig. S25) demonstrate that the potential HER-active sites are located on the surfaces of the Pt NPs. Crystal Orbital Hamilton Population (COHP) analysis (Fig. 4f and S26) demonstrates a 31% reduction in Pt–H bond strength (ICOHP: –1.34 eV at 5% strain to –0.92 eV at 7% strain), which is originated from the more crowded d -orbital on Pt due to the electron transfer, consistent with the improved charge transfer under higher strain. This bond-weaken directly facilitates hydrogen desorption, as evidenced by free-energy calculations across five strained configurations (Fig. 4g). While the unstrained system exhibits excessive hydrogen binding ($\Delta G_H = -0.61$ eV), progressive lattice expansion raises ΔG_H to an optimal –0.32 eV at 7% strain. The attenuated Pt–H interactions, together with the amplified electron supply to Pt sites by LMCT charge separation benefit desorption kinetics and hydrogen adsorption capacity toward enhanced performance.

We then performed a comparative measurement of photocatalytic performance with controlled flow condition by hydrocyclone cycling (Fig. 4h). Precise modulation of flow rates (10–40 L/min) elicits a threshold-activated catalytic amplification effect, where hydrogen evolution rates surge by 59% (8.0 to 12.7 mmol/h) within the 20–30 L/min regime, coinciding with the optimal shear-induced lattice restructuring window. In contrast, subcritical (10–20 L/min: +1.3 mmol/h) or saturated (30–40 L/min: +1.9 mmol/h) flows yield only marginal gains. It confirms that hydrodynamic shear dynamically reconfigures Pt surface coordination on catalyst particles, synchronously aligning interfacial strain fields to expedite charge separation and amplify photocatalytic hydrogen generation. Building on the established multiscale mechanism of hydrocyclone-enhanced photocatalytic hydrogen generation, we envision an industrial-scale system scaled up 100-fold with 300 transparent hydrocyclones in parallel, demonstrating the remarkable scalability of this technology (Fig. S30). The compact system occupies only 10 m², utilizing industrial waste pressure to deliver photocatalyst-laden feed solution at 240 m³/h without additional electrical power requirements. Solar irradiation concentrated by Fresnel lenses is transmitted through optical fibers for synchronous illumination, while the feed pressure generates intense turbulent shear that significantly enhances mass transfer and photocatalytic efficiency. This configuration can potentially achieve 27 L/h hydrogen production through efficient centrifugal gas-liquid separation. Compared to conventional plate-type reactors, this hydrocyclone-based system can demonstrate superior efficiency

through its compact footprint and enhanced mass transfer characteristics inherent to cyclonic flow patterns.

Discussion

In this work, we first analyzed the mechanism of the macroscopic flow field in the cyclone inducing the microscopic strain of the catalyst through CFD-DEM simulations, finite element modeling, and AIMD simulations. Combined with DFT calculation, we analyzed the changes in photocatalytic performance under strain, discovering that the shear-induced lattice strain is the key driving force of the threshold-activated surge in hydrogen evolution rates. We constructed a hydrocyclone based photocatalytic reactor based on the intrinsic correlation framework model of cyclone-excited photocatalysis. The results showed that at the optimal rotational speed, the hydrogen production rate of 270 mL/h and an STH efficiency exceeding 5% can be achieved. Overall, our integrated experimental-theoretical approach has established a powerful blueprint for the process intensification design of scalable photocatalytic reactors tailored for large-scale industrial hydrogen production, thereby enabling the optimization of industrial-scale hydrogen production processes under continuous flow operation.

Methods

Synthesis of photocatalysts

All reagents and solvents utilized in the synthesis were of analytical grade and used without further purification unless otherwise specified. The synthesis of 1,3,5-triformylphloroglucinol (Tp) was performed under an inert atmosphere by adding 90 mL of trifluoroacetic acid (CF₃COOH) to a mixture of hexamethylenetetramine (15.098 g, 108 mmol) and phloroglucinol (6.014 g, 49 mmol). The reaction mixture was heated at 100 °C for 2.5 h, followed by the addition of 150 mL of 3 M hydrochloric acid (HCl) and continued heating at 100 °C for an additional hour. After cooling to room temperature, the mixture was filtered through Celite and extracted with dichloromethane. The organic layer was dried over anhydrous magnesium sulfate, filtered, and concentrated via rotary evaporation to yield a yellow powder. This crude product was purified by sublimation at 150 °C to obtain a white solid. The product was characterized by ¹H NMR (400 MHz, CDCl₃, δ): -13.770 (3H, s), -9.817 (3H, s) ppm.

TpPa-COF was prepared in an aqueous surfactant/polymer medium.⁵⁶ Briefly, cetylpyridinium bromide (CPB, 15 mL, 1 mg·mL⁻¹) was placed in a 50 mL round-bottom flask and agitated at 500 rpm. Polyvinylpyrrolidone (PVP, 40 mg) was then dissolved in this solution, followed by the addition of Pa (24 mg, 0.225 mmol) after 10 min of stirring. In parallel, Tp (31.5 mg, 0.15 mmol) was sonicated in dichloromethane (3.5 mL) to form a clear organic phase, which was subsequently introduced into the aqueous phase by dropwise addition at 0.5 mL·min⁻¹. The biphasic mixture was maintained under stirring at ambient temperature for 1 h to afford a red emulsion. The product was isolated by centrifugation (11000 rpm, 20 min) and rinsed three times with methanol (30 mL) and tetrahydrofuran (30 mL). Finally, the collected red solid was dried under vacuum at 100 °C for 12 h, yielding 45.5 mg of TpPa-COF (95.3% yield).

To prepare the Pt-COF, 100 mg of TpPa-COF was dispersed in 100 mL of chilled deionized water (5 °C), followed by the addition of 754 μL of H₂PtCl₆ solution (3981.7 mg·L⁻¹). The suspension was stirred vigorously and irradiated under full-spectrum light (≥ 350 nm, 100 mW·cm⁻²) for 1 h. The resulting dark red solid was collected by filtration and washed with deionized water until the filtrate reached neutral pH. The product was vacuum-dried at 60 °C to afford Pt-COF (82.3 mg, 82.3% yield).

The tracer particles were synthesized by directly dropping sodium alginate solution into a calcium lactate solution, where cross-linking occurred. By controlling the stirring speed during droplet formation, the resulting tracer particles were maintained at ~3 mm in diameter, with a measured density of 1.40 g/cm³. In contrast, the actual

catalyst particles have a density of 1.63 g/cm³ (measured via a degassing method). However, when considering the binary packing of catalyst particles in solution, the solid volume fraction in the aggregated state is ~64%. Given that the true density of the catalyst material—measured via a densimeter—is 1.63 g/cm³, the resulting aggregate density is around 1.40 g/cm³, aligning closely with the density of our tracer particles. In addition, the tracer microspheres possess a relatively low Young's modulus to allow clear observation of deformation.

Characterization

Powder X-ray diffraction (XRD) patterns were recorded using a Rigaku Ultima IV system to elucidate the catalysts' crystallographic structures. Morphological and microstructural features were investigated via scanning electron microscopy (SEM, Zeiss Gemini 300) and transmission electron microscopy (TEM, Tecnai G2 F20), respectively. Elemental composition and chemical states were determined by X-ray photoelectron spectroscopy (XPS) on a PHI 5000CESCA spectrometer equipped with Al Kα radiation (1486.6 eV); the C 1s peak at 284.8 eV served as the reference for binding energy calibration, enabling both qualitative and quantitative elemental analyses. Fourier-transform infrared (FTIR) spectroscopy (Bruker Vertex 70) was employed to identify surface functional groups, and UV-vis absorption spectra were measured using a Shimadzu UV-3600 spectrophotometer.

Photocatalytic measurements

A typical photocatalytic hydrogen production experiment and subsequent data collection were conducted using the hydrocyclone-based reactor developed in this work. First, a precursor solution was prepared by dispersing 540 mg of catalyst in 500 mL of ultrapure water, together with 317 g (1.8 mol) of ascorbic acid as a sacrificial agent; the mixture was sonicated for 1 h. The reactor was then rinsed with 10 L of ultrapure water for 30 min and drained. Afterward, 17.5 L of ultrapure water and the precursor solution were introduced into the reactor, and the pump flow rate was set to 40 L min⁻¹ under continuous N₂ purging. Cooling water at 5 °C was circulated for 60 min. Subsequently, the light source was switched on and the N₂ supply was stopped, establishing a slight positive pressure inside the reactor. Every 30 min, a gas-sampling syringe was inserted into the top sampling port; upon opening the port valve, the syringe was allowed to fill to the 20 mL mark under the reactor pressure, after which the valve was closed and the syringe removed. Gas samples were analyzed using a GC7920 gas chromatograph equipped with TCD and FID detectors (Ar as carrier gas). All experiments were performed in triplicate.

Headspace definition and calibration

Prior to each run, the reactor is completely filled with the preset feed solution (~20 L prepared in advance) while the circulation pump is operated at a low flow rate to remove residual bubbles, until overflow occurs and the internals are fully liquid-filled. We then open the bottom drain valve and withdraw 500 mL of liquid using a calibrated volumetric cylinder, which defines a fixed gas headspace of V_{HS} = 500 mL ± 5 mL.

Sampling and analysis

At a given time t_k , we sample 1 mL of the headspace using a gas-tight microsyringe and record the headspace absolute pressure P_k from the in-line gauge and the temperature T_k . The sample is injected into the gas chromatograph, and the H₂ mole fraction y_k is obtained from a calibration curve. The instantaneous moles of hydrogen in the headspace are computed with the ideal-gas relation:

$$n_k(\text{H}_2) = \frac{(P_k - P_{\text{H}_2\text{O}}(T_k)) V_{\text{HS}}}{RT_k} \times y_k \quad (4)$$

where $P_{\text{H}_2\text{O}}(T_k)$ is the saturated water-vapor pressure at T_k and R is the gas constant. The 1 mL sampling volume is $<0.2\%$ of V_{HS} ; we correct P_k and y_k for this removal in the data reduction.

Yield and rate over extended operation

Measurements are taken every 30 min. The cumulative hydrogen yield over any interval is evaluated as the telescoping sum of headspace increases:

$$N_{\text{H}_2}(t_j) = \sum_{k=1}^j [n_k(\text{H}_2) - n_{k-1}(\text{H}_2)] \quad (5)$$

and the average production rate over $[t_{k-1}, t_k]$ is $r_k = (n_k - n_{k-1})/\Delta t$. To prevent saturation and to maintain consistent sensitivity, operation is organized into 3.5 h cycles (8 analyses per cycle). At the end of each cycle, the headspace is purged with Ar for 10 min to reduce residual H_2 ; the first analysis of the next cycle defines the new baseline ($n_0 \approx 0$). The hydrogen removed during purge is accounted for by closing the material balance on each cycle.

Temperature test

A temperature probe mounted on the reservoir recorded the bulk liquid temperature every 30 min. With the chiller supplying cooling water at 4 °C, the illuminated reactor maintained a stable bulk temperature of 30 ± 1 °C. Representative temperature-time traces from three independent runs (September 18, 22, and 25, 2025) show that thermal steady state is reached within ~2 h after start-up and exhibits no drift during extended operation.

Computational methods

A two-phase flow model was established to simulate a liquid (water) and solid (catalyst agglomerates) system (Table S1). The average agglomerate particle size was set to 40 μm . An inlet boundary condition of velocity-inlet was employed, while the overflow and underflow were defined as outflow boundaries. Turbulence intensity at the inlet (4.3%) was estimated using the empirical correlation $I = 0.16(\text{Re}_D)^{-1/8}$. Non-equilibrium wall functions were applied to the reactor walls to capture near-wall effects. The hydrocyclone fluid domain was constructed in SOLIDWORKS 2022 (Dassault Systemes, France), and meshing and CFD simulations were conducted using ANSYS Fluent (2020 R, ANSYS, USA).

In a representative hierarchical multiscale modeling workflow, discrete element method (DEM) simulations revealed a maximum contact force of 1.8×10^{-6} N exerted on the agglomerates. This value was then used in ABAQUS to build a 40 μm “micro-cluster,” composed of COF particles with a bulk Young’s modulus of 5 GPa and a Poisson’s ratio of 0.3.⁵⁷ The micro-cluster porosity was set to 0.5, resulting in an effective Young’s modulus of 1.75 GPa and a Poisson’s ratio of 0.27 for the overall agglomerate (obtained via homogenization theory). Under a tensile load of 1.8×10^{-6} N, the cluster exhibited a maximum surface displacement of -1.75 Å. A 3 μm zone at the cluster surface was then extracted as an RVE comprising 120 primary particles (each 600 nm in diameter). Imposing the 1.75 Å displacement on the RVE revealed a local displacement of 2.13 Å in individual catalyst particles.

For atomic-level calculations, AIMD simulations were carried out using CP2K’s Quickstep module under an unrestricted Kohn-Sham (UKS) scheme. The BASIS_MOLOPT, BASIS_MOLOPT_UCL, and GTH_POTENTIALS libraries were employed for basis sets and pseudopotentials. Self-consistent field (SCF) convergence was enforced at 1×10^{-6} with an orbital transformation method and conjugate gradient minimizer. The exchange-correlation interaction was described by the Perdew-Burke-Ernzerhof (PBE) functional, and the density cutoff was set to 400 Ry with a relative cutoff of 60 Ry across four MGRID levels. Molecular dynamics were performed under an NVT ensemble at 330 K

using a 1 fs time step, each configuration running for 1000 steps before incrementally expanding the lattice by 2% biaxially. This cycle continued until the COF ring fracture, indicated by a pronounced energy fluctuation, at which point the simulation halted.

Additional standard calculations were conducted with the Vienna Ab initio Simulation Package (VASP).⁵⁸ A plane-wave cutoff energy of 450 eV was used, with a convergence criterion of 0.01 eV/Å. The Perdew-Burke-Ernzerhof (PBE) functional within the Generalized Gradient Approximation (GGA) framework handled exchange-correlation interactions.⁵⁹ For geometry optimization, a $2 \times 2 \times 1$ k-mesh was utilized, while density of states calculations employed a $6 \times 6 \times 1$ k-mesh. Post-processing was performed with Multiwfn (version 3.8).⁶⁰ Convergence test data are shown in Fig. S27.

In this work, the apparent quantum yield (AQY) at 420 nm is calculated from the ratio of photogenerated hydrogen molecules to incident photons as.

$$\text{AQY}(\%) = \frac{2 \times N_{\text{H}_2}}{N_{\text{photons}}} \times 100 \quad (6)$$

where N_{H_2} is the number of generated hydrogen molecules, N_{photons} is the number of incident photons, and the factor of 2 arises from the two electrons needed for one H_2 molecule. For the purpose of illustration, please refer to the calculation example, which can be found in the supplementary information.

The solar-to-hydrogen (STH) efficiency, used for device-level energy accounting in scaled hydrogen-production reactors, is determined by the ratio of the energy stored in the produced hydrogen to the incident solar energy, expressed as

$$\text{STH} = \frac{r_{\text{H}_2} \times \mathcal{E}_{\text{H}_2}}{P_{\text{sun}} \times S} \quad (7)$$

where r_{H_2} is the hydrogen production rate, \mathcal{E}_{H_2} is the energy content of hydrogen, P_{sun} is the solar energy flux, and S is the irradiated area.⁶¹

For the thermodynamics of the HER, we calculate the Gibbs free energy $\Delta G_{\text{H}^{\cdot}}$:

$$\Delta G_{\text{H}^{\cdot}} = E_{\text{H}^{\cdot}} - E_{\text{surface}} - \frac{1}{2}E_{\text{H}_2} + \Delta E_{\text{ZPE}} + \Delta U(0 \rightarrow T) - T\Delta S_{\text{H}} \quad (8)$$

where $E_{\text{H}^{\cdot}}$ is the total energy of the catalyst surface with an adsorbed hydrogen atom, E_{surface} is the total energy of the pristine catalyst surface, E_{H_2} is the total energy of gas-phase H_2 , ΔE_{ZPE} is the zero-point energy correction, $\Delta U(0 \rightarrow T)$ is the $0 \rightarrow T$ thermal internal-energy correction, T is the temperature, and ΔS_{H} is the entropy change upon H adsorption. All thermodynamic corrections were performed using VASPKIT to ensure accurate zero-point energy and entropic contributions.⁶² Detailed data are presented in Table S4.

Data availability

All data supporting the findings of this study are available from the source data. The relevant DFT optimised structures are provided in the Supplementary Data 1. Source data are provided with this paper.

References

- Rahman, M. Z., Edvinsson, T. & Gascon, J. Hole utilization in solar hydrogen production. *Nat. Rev. Chem.* **6**, 243–258 (2022).
- Loeb, S. K. et al. The technology horizon for photocatalytic water treatment: sunrise or sunset? *Environ. Sci. Technol.* **53**, 2937–2947 (2019).
- Chen, G. et al. Solar-driven production of renewable chemicals via biomass hydrogenation with green methanol. *Nat. Commun.* **16**, 665 (2025).

4. Imran, S. & Hussain, M. Emerging trends in water splitting innovations for solar hydrogen production: analysis, comparison, and economical insights. *Int. J. Hydrog. Energy* **77**, 975–996 (2024).
5. Qiao, M. et al. The green hydrogen implementation gap. *Nat. Chem. Eng.* **10**, 110–123 (2025).
6. Jiang, J. et al. Water resource recovery facilities empower the electrolytic hydrogen economy. *Environ. Sci. Technol.* **58**, 22124–22134 (2024).
7. Msheik, M., Rodat, S. & Abanades, S. Solar methane pyrolysis in a liquid metal bubble column reactor: effect of medium type and gas injection configuration. *J. Anal. Appl. Pyrolysis* **183**, 106756 (2024).
8. Guan, D. et al. Comprehensive study on catalytic coating tubular reactor with electromagnetic induction heating for hydrogen production through methanol steam reforming. *Int. J. Hydrog. Energy* **50**, 1–17 (2024).
9. Eran, T. N. et al. Kinetics, catalyst design, and hydrodynamic analysis in Fischer-Tropsch synthesis: fixed bed vs fluidized bed reactors. *Chem. Eng. J.* **500**, 156796 (2024).
10. Fu, H. et al. A scalable solar-driven photocatalytic system for separated H₂ and O₂ production from water. *Nat. Commun.* **16**, 990 (2025).
11. Nishiyama, H. et al. Photocatalytic solar hydrogen production from water on a 100-m² scale. *Nature* **598**, 304–307 (2021).
12. Gunawan, D. et al. Materials advances in photocatalytic solar hydrogen production: integrating systems and economics for a sustainable future. *Adv. Mater.* **36**, 2404618 (2024).
13. Mani, P. et al. Scaling up of photocatalytic systems for large-scale hydrogen generation. *Appl. Phys. Rev.* **12**, 011303 (2025).
14. Rej, S. et al. Well-defined Cu₂O photocatalysts for solar fuels and chemicals. *J. Mater. Chem. A* **9**, 5915–5951 (2021).
15. Rossetti, I. & Compagnoni, M. Chemical reaction engineering, process design and scale-up issues at the frontier of synthesis: Flow chemistry. *Chem. Eng. J.* **296**, 56–70 (2016).
16. The pathway to process scale-up. *Nat. Chem. Eng.* **1**, 387–388 (2024).
17. Reynes, J. F., Isoni, V. & Garcia, F. Tinkering with mechanochemical tools for scale up. *Angew. Chem. Int. Ed.* **62**, e202300819 (2023).
18. Luterbacher, J. et al. Connecting scales in reaction engineering. *Nat. Chem. Eng.* **2**, 156–159 (2025).
19. Liu, W. et al. Efficient hydrogen production from wastewater remediation by piezoelectricity coupling advanced oxidation processes. *Proc. Natl. Acad. Sci.* **120**, e2218813120 (2023).
20. Chen, C. et al. Pressure drop and flow distribution in a group of parallel hydrocyclones: ZZ-type arrangement. *Sep. Purif. Technol.* **108**, 15–27 (2013).
21. Lv, W. et al. UU-type parallel mini-hydrocyclone group for oil-water separation in methanol-to-olefin industrial wastewater. *Chem. Eng. Process.-Process Intensif.* **149**, 107846 (2020).
22. Liu, Y. et al. Three-phase hydrocyclone separator-A review. *Chem. Eng. Res. Des.* **100**, 554–560 (2015).
23. Lv, W. et al. Process of removing heavy metal ions and solids suspended in micro-scale intensified by hydrocyclone. *J. Clean. Prod.* **263**, 121533 (2020).
24. Jiang, Z. et al. Hydrogen production by suspension self-rotation enhanced pyrolysis of sludge particles in cyclone. *Water Res.* **275**, 123198 (2025).
25. Li, S. et al. Separation and recovery of waste heat from millimeter-sized blast furnace slag in cyclone separators. *Sep. Purif. Technol.* **367**, 132908 (2025).
26. Kim, K. S. et al. Continuous synthesis of high-entropy alloy nanoparticles by in-flight alloying of elemental metals. *Nat. Commun.* **15**, 1450 (2024).
27. Han, J. Y., La Fiandra, J. N. & DeVoe, D. L. Microfluidic vortex focusing for high throughput synthesis of size-tunable liposomes. *Nat. Commun.* **13**, 6997 (2022).
28. Liu, W. et al. Hydroenergy inspiring large-scale piezoelectric catalysis for seawater hydrogen evolution. *Angew. Chem. Int. Ed.* **64**, e202504749 (2025).
29. Wang, Z. et al. A contact-electro-catalysis process for producing reactive oxygen species by ball milling of triboelectric materials. *Nat. Commun.* **15**, 757 (2024).
30. Mao, X. et al. Strain engineering of electrocatalysts for hydrogen evolution reaction. *Mater. Horiz.* **10**, 340–360 (2023).
31. Chen, K. et al. Atomic-scale strain engineering of atomically resolved Pt clusters transcending natural enzymes. *Nat. Commun.* **15**, 8346 (2024).
32. Lin, J. & Zhang, N. Constructing strain in electrocatalytic materials for CO₂ reduction reactions. *Green Chem.* **26**, 4449–4467 (2024).
33. Chen, A. et al. Metal oxide nanocomposites: a perspective from strain, defect, and interface. *Adv. Mater.* **31**, 1803241 (2019).
34. Wang, X. et al. Interfacial chemical bond and internal electric field modulated Z-scheme Sv-ZnIn₂S₄/MoSe₂ photocatalyst for efficient hydrogen evolution. *Nat. Commun.* **12**, 4112 (2021).
35. Cambie, D. et al. Applications of continuous-flow photochemistry in organic synthesis, material science, and water treatment. *Chem. Rev.* **116**, 10276–10341 (2016).
36. Yu, F. et al. Molecular engineering of donor-acceptor conjugated polymer/g-C₃N₄ heterostructures for significantly enhanced hydrogen evolution under visible-light irradiation. *Adv. Funct. Mater.* **28**, 1804512 (2018).
37. Liu, X. et al. Hydroxylated organic semiconductors for efficient photovoltaics and photocatalytic hydrogen evolution. *Energy Environ. Sci.* **16**, 4065–4072 (2023).
38. He, X. et al. Engineering a self-grown TiO₂/Ti-MOF heterojunction with selectively anchored high-density Pt single-atomic cocatalysts for efficient visible-light-driven hydrogen evolution. *Angew. Chem.* **135**, e202217439 (2023).
39. Wang, Y. et al. Molecular engineering for modulating photocatalytic hydrogen evolution of fully conjugated 3D covalent organic frameworks. *Angewandte Chemie International Edition*, **63**, e202404726 (2024).
40. Xu, T. et al. Simultaneous defect passivation and co-catalyst engineering leads to superior photocatalytic hydrogen evolution on metal halide perovskites. *Angewandte Chemie International Edition*, **63**, e202409945 (2024).
41. Guo, Y. et al. Perylenetetra-carboxylic acid nanosheets with internal electric fields and anisotropic charge migration for photocatalytic hydrogen evolution. *Nat. Commun.* **13**, 2067 (2022).
42. Zhou, P. et al. Solar-to-hydrogen efficiency of more than 9% in photocatalytic water splitting. *Nature* **613**, 66–70 (2023).
43. Goto, Y. et al. A particulate photocatalyst water-splitting panel for large-scale solar hydrogen generation. *Joule* **2**, 509–520 (2018).
44. Schröder, M. et al. Hydrogen evolution reaction in a large-scale reactor using a carbon nitride photocatalyst under natural sunlight irradiation. *Energy Technol.* **3**, 1014–1017 (2015).
45. Wei, Q. et al. Experimental study on direct solar photocatalytic water splitting for hydrogen production using surface uniform concentrators. *Int. J. Hydrog. Energy* **43**, 13745–13753 (2018).
46. Hisatomi, T. & Domen, K. Reaction systems for solar hydrogen production via water splitting with particulate semiconductor photocatalysts. *Nat. Catal.* **2**, 387–399 (2019).
47. He, T. & Zhao, Y. Covalent organic frameworks for energy conversion in photocatalysis. *Angew. Chem. Int. Ed.* **62**, e202303086 (2023).
48. Dong, P. et al. Platinum single atoms anchored on a covalent organic framework: boosting active sites for photocatalytic hydrogen evolution. *Acs Catal.* **11**, 13266–13279 (2021).
49. Yuan, X. et al. Progress in preparation and application of sodium alginate microcapsules. *Chem. Ind. Eng. Prog.* **41**, 3103 (2021).

50. Budarapu, P. R. et al. Multiscale modeling of material failure: theory and computational methods. *Adv. Appl. Mech.* **52**, 1–103 (2019).
51. Vernerey, F., Liu, W. K. & Moran, B. Multi-scale micromorphic theory for hierarchical materials. *J. Mech. Phys. Solids* **55**, 2603–2651 (2007).
52. Zhao, J., Zhao, S. & Luding, S. The role of particle shape in computational modelling of granular matter. *Nat. Rev. Phys.* **5**, 505–525 (2023).
53. Li, Y. et al. In situ photodeposition of platinum clusters on a covalent organic framework for photocatalytic hydrogen production. *Nat. Commun.* **13**, 1355 (2022).
54. Zhou, F. et al. Enhanced solar-driven CO₂ conversion: the role of Yb-doped CuInS₂ quantum dots on g-C₃N₄ nanosheets. *Appl. Catal. B: Environ. Energy* **362**, 124716 (2025).
55. Huang, Z. & Boulatov, R. Chemomechanics: chemical kinetics for multiscale phenomena. *Chem. Soc. Rev.* **40**, 2359–2384 (2011).
56. Zhang, J. et al. Biomimetic synthesis of vesicular covalent organic frameworks by gemini surfactants for in-situ enzyme cascade immobilization. *Nat. Commun.* **16**, 6046 (2025).
57. Teng, Z. et al. Atomically isolated Sb(CN)₃ on sp²-c-COFs with balanced hydrophilic and oleophilic sites for photocatalytic CH activation. *Sci. Adv.* **10**, ead15432 (2024).
58. Kresse, G. & Furthmüller, J. Efficiency of ab-initio total energy calculations for metals and semiconductors using a plane-wave basis set. *Comput. Mater. Sci.* **6**, 15–50 (1996).
59. Perdew, J. P., Burke, K. & Ernzerhof, M. Generalized gradient approximation made simple. *Phys. Rev. Lett.* **77**, 3865 (1996).
60. Lu, T. A. et al. Comprehensive electron wavefunction analysis toolbox for chemists, Multiwfn. *J. Chem. Phys.* **8**, 161 (2024).
61. Holmes-Gentle, I. et al. Kilowatt-scale solar hydrogen production system using a concentrated integrated photoelectrochemical device[J]. *Nat. Energy* **8**, 586–596 (2023).
62. Wang, V. et al. VASPkit: A user-friendly interface facilitating high-throughput computing and analysis using VASP code. *Comput. Phys. Commun.* **267**, 108033 (2021).
- evaluations, and maintained comprehensive experimental documentation. C.C. and J.L. conducted theoretical computations pertaining to mechanical characterization. P.F. established the research methodology and analysis protocols. M.M., W.L., and Z.Z. contributed to critical interpretation of results through scientific discourse. J.L., X.Y., and H.W. supervised research activities, provided intellectual guidance, and administered project coordination.

Competing interests

The authors declare no competing interests

Additional information

Supplementary information The online version contains supplementary material available at <https://doi.org/10.1038/s41467-026-68895-2>.

Correspondence and requests for materials should be addressed to Jianping Li, Xuejing Yang or Hualin Wang.

Peer review information *Nature Communications* thanks the anonymous, reviewer(s) for their contribution to the peer review of this work. A peer review file is available.

Reprints and permissions information is available at <http://www.nature.com/reprints>

Publisher's note Springer Nature remains neutral with regard to jurisdictional claims in published maps and institutional affiliations.

Open Access This article is licensed under a Creative Commons Attribution-NonCommercial-NoDerivatives 4.0 International License, which permits any non-commercial use, sharing, distribution and reproduction in any medium or format, as long as you give appropriate credit to the original author(s) and the source, provide a link to the Creative Commons licence, and indicate if you modified the licensed material. You do not have permission under this licence to share adapted material derived from this article or parts of it. The images or other third party material in this article are included in the article's Creative Commons licence, unless indicated otherwise in a credit line to the material. If material is not included in the article's Creative Commons licence and your intended use is not permitted by statutory regulation or exceeds the permitted use, you will need to obtain permission directly from the copyright holder. To view a copy of this licence, visit <http://creativecommons.org/licenses/by-nc-nd/4.0/>.

© The Author(s) 2026

Acknowledgements

This work was supported by National Natural Science Foundation of China (52400080).

Author contributions

D.Y. conceived the original concept, designed the experimental framework, and developed the multiscale computational model. Y.Y. and F.Z. performed catalyst synthesis, conducted data analytics of experimental results, and executed DFT simulations. Z.D. engineered the hydrogen production reactor system, carried out catalytic performance